Influence of wettability conditions on slow evaporation in two-dimensional porous media

O. Chapuis and M. Prat*
Institut de Mécanique des Fluides de Toulouse, UMR CNRS-INP/UPS No. 5502,
Avenue du Professeur Camille Soula, 31400 Toulouse, France
(Received 22 September 2006; revised manuscript received 5 February 2007; published 30 April 2007)

We study numerically the influence of the wettability condition on slow evaporation in two-dimensional pore square networks of aspect ratio 1. We show how evaporation in a hydrophobic network can be simulated numerically by combining imbibition rules and the computation of diffusion transport in the gas phase. Then we conduct a statistical study of drying in hydrophilic or hydrophobic networks based on pore network simulations. We concentrate on the situation where the external transfer resistance and liquid film effect are negligible and the invasion is dominated by capillary effects. It is found that drying in a hydrophilic network is significantly faster than in a hydrophobic one. The dimensionless overall drying time is found to be network size dependent, approaching exponentially a limit for large size hydrophilic networks. The dimensionless average overall drying time is 0.93 and 0.75 in hydrophobic and hydrophilic large networks, respectively. Other properties, such as the overall saturation and the evaporation flux (through the concept of equivalent flat front position) are also studied. In a last part the impact of liquid film flow on the overall drying time fluctuation is briefly investigated for the case of hydrophilic networks. It is found that the films dampen the drying time fluctuations.

DOI: 10.1103/PhysRevE.75.046311 PACS number(s): 47.56.+r

I. INTRODUCTION

Evaporation in porous media is a process of significant interest in relation with numerous applications such as the drying of many products, the recovery of volatile hydrocarbons from underground oil reservoirs, or the remediation of contaminated soils by vapor extraction. In these applications, the liquid is generally wetting and drying can then be regarded as a drainage process, where the evaporating wetting liquid is replaced by a nonwetting gas. This case has been the subject of many studies in recent years within the framework of pore–network models and invasion percolation theory, e.g., [1,2] and references therein. However, there are also important applications in which evaporation occurs in a hydrophobic porous medium. For example, buildings stones can be rendered hydrophobic in order to limit the salt weathering hazards due to the salt crystal formations resulting from evaporation,[3]. PEFCs (polymer electrolyte fuel cells) are another example in which evaporation, as well as other two-phase flow processes, takes place in hydrophobic (teflonized) porous (fibrous) layers. A proper understanding and modeling of two phase flows, including evaporation, in teflonized systems is important in relation with the problem of water management of PEFCs [4].

Throughout the text the wettability of the system is characterized by the contact angle θ measured in the dense phase, i.e., liquid water in the present context. Hence θ is lower than 90° in a hydrophilic pore network and greater than 90° in a hydrophobic one. The change in wettability from a hydrophilic material to a hydrophobic one is expected to lead to a major change in terms of invasion pattern and therefore also in terms of evaporation rate. In this paper, we study this change and its impact on drying rates in the quasistatic limit, i.e., when the pressure evolution in the liquid phase is only due to capillary effects. By analogy with quasistatic mechanical displacements, e.g., [5], we expect invasion percolationlike fractal patterns in the hydrophilic network whereas a flat invasion front is expected in the hydrophobic case. The study is conducted for two-dimensional (2D) square networks of interconnected ducts of rectangular cross section under the assumption of dilute concentration of water vapor in the gas phase (evaporation at temperatures close to the ambient temperature), see Fig. 1 for a sketch of the network.

The paper is organized as follows. In Sec. II the pore–network models of drying developed to simulate the evaporation process in hydrophilic or hydrophobic networks are presented. The impact of the wettability condition on drying is analyzed in Sec. III through pore network simulations in the hydrophilic (neglecting the film effect) or hydrophobic network. In Sec. IV, the effect of corner films in hydrophilic networks is briefly investigated.

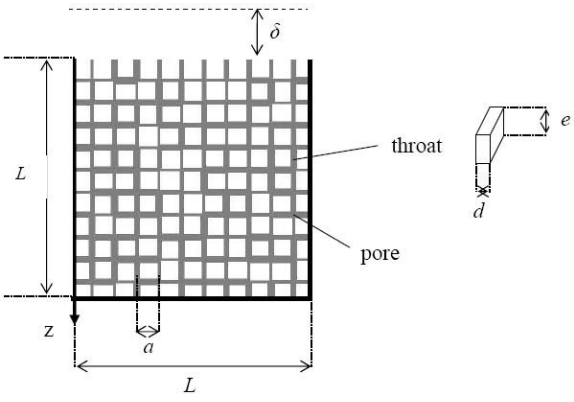

FIG. 1. Sketch of 2D square network. Pore space in gray.

*Corresponding author. Electronic address: prat@imft.fr

II. PORE–NETWORK MODELS OF EVAPORATION

A. Network geometry and external boundary condition

For simplicity, we consider a situation where heat transfer can be neglected. This corresponds typically to evaporation of a not too volatile liquid at the ambient temperature. The pore space is conceptualized as a network of randomly sized pores (sites) joined by randomly sized throats (bonds). As in many previous works, a square lattice (of regular spacing a) is used in this paper, see Fig. 1. The bonds are straight channels of rectangular cross section. In this model, every pore and throat have the same depth e whereas the throat width d is distributed randomly according to a uniform distribution law in the range $[d_{\min}, d_{\max}]$. The length ℓ of each throat is a fraction of the distance between two sites of network: $\ell = \beta a$ (we have taken $\beta = 0.46$ in the simulations but the statistical results are not sensitive to the particular value chosen for β). Pores are located on the sites of network. The volume of a pore is determined from the geometric characteristics of adjacent throats; see Appendix in [6] for more details. As depicted in Fig. 1, three edges of the network are impervious (no mass transfer at these boundaries). The vapor escapes through the remaining open edge (top edge in Fig. 1). Initially, the network is completely saturated by liquid water.

We assume that the external mass flux density can be expressed as

$$j = D\frac{M_v}{RT}\frac{(P_{vi} - P_{v\infty})}{\delta}, \tag{1}$$

where D, M_v, R, T, P_{vi}, $P_{v\infty}$ are the diffusion coefficient of water vapor, vapor molar mass, gas constant, ambient temperature, vapor partial pressure at the porous surface, and vapor partial pressure in the surrounding air, respectively. In Eq. (1), δ is the characteristic length scale of external transfer ($\approx$mass boundary layer average thickness).

B. Hydrophilic network

As mentioned in the Introduction, evaporation in hydrophilic networks has been the subject of several studies since the experiments by Shaw [7] indicating that evaporation could be analyzed as an invasion percolation process. A pore–network model for studying drying patterns and drying rates was then first proposed in [6] for slow evaporation of a single component liquid when thermal effects can be ignored. This two-dimensional model takes into account capillary effects through an invasion percolation (IP) rule [8], and the transport by diffusion in the gas phase of the evaporating species. Since this first attempt, increasingly sophisticated models have been developed so as to take into account gravity effects [9], viscous effects [10], thermal effects [11], film effects [12,13], and binary liquids [14]. Three-dimensional versions, though not including all effects, have also been developed [15]. Experiments with etched networks have led to satisfactory comparisons in terms of drying patterns and have shown the strong influence of film flows on drying rates [16]. The analysis of drying patterns can be performed using invasion percolation concepts and this has been performed in some details, e.g.,[17], notably in relation with the experimental results reported in [7] indicating that the viscous effects stabilize the invasion. The film effect refers to the influence of liquid films trapped by capillarity within the corners or wedges of pore space after invasion of pore bulk by the gas phase. A sketch of this type of film is shown in Fig. 2 for a duct of square cross section.

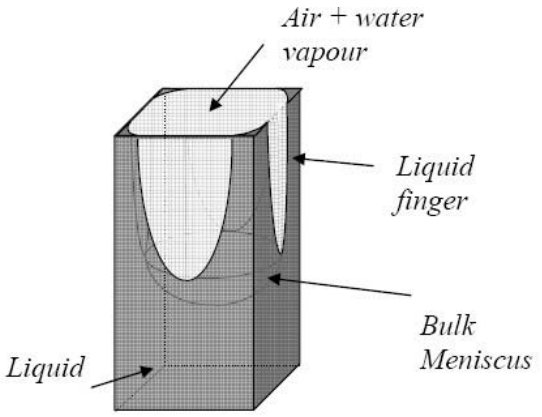

FIG. 2. When the main meniscus recedes into a hydrophilic duct of polygonal cross section, the corners remain occupied by liquid water films due to the capillary effect (if $\theta < \theta_c$).

Owing to the influence of liquid film flows, it is now well-established that a change in contact angle may have a dramatic effect on drying rates [12,13]. When the pore geometry and the contact angle are such that film flows cannot develop, drying is very slow since the transport of water molecules from the menisci within the porous materials to the porous medium surface is by diffusion within the gas phase. By contrast, as shown in [12] or [13], the flow in liquid films trapped in the corners of the "gas" pores can represent a much more efficient transport mechanism than diffusion, which leads to a much faster drying compared to the situation where diffusion in the gas phase is the dominant transport mechanism in the region invaded by air. As discussed in [13], for a given pore space geometry, it is expected that film flows cannot develop above a critical contact angle θ_c because liquid capillary trapping in pore space corners is not possible for $\theta > \theta_c$. The value of θ_c depends on the pore space geometry. For a real porous medium, this concept should be understood in some average sense since the details of the pore space geometry may vary spatially as well as the local wettability condition. In our case, for ducts of rectangular cross section, $\theta_c = 45°$. Experiments on etched networks [16] indicate, however, that the invasion pattern is not very sensitive to the effect of films provided that viscous effects can be neglected in the fully saturated liquid pores, an assumption that is made throughout the present paper, see [13] for more details. In other terms, the phase distribution can be predicted neglecting the film effect but not the drying rate. When the viscous effects can be neglected in the liquid saturated regions, a simple model to describe the evolution of phase distribution during slow drying is to apply the invasion percolation (IP) algorithm to each cluster present in the pore network [6]. However, using the IP algorithm is not necessarily valid over the full range of contact angle (0, 90°) corresponding to hydrophilic materials. By analogy with the re-

TABLE I. Summary of various evaporation regimes considered in this paper.

Regime	I	II	III	Hydrophobic
Contact angle of liquid	$0 \leqslant \theta < \theta_c < 90°$	$\theta_c \leqslant \theta < \theta_{c2} < 90°$	$\theta_{c2} \leqslant \theta < 90°$	$90° < \theta$
Network wettability	Hydrophilic	Hydrophilic	Hydrophilic	Hydrophobic
Mechanical liquid invasion equivalent process	Drainage	Drainage	Drainage	Imbibition
Main characteristics of evaporation model	IP+liquid corner films+binary diffusion in gas phase	IP+binary diffusion in gas phase (no film effect)	Throat and pore invasion mechanisms are distinct events+binary diffusion in gas phase (no film effect)	Imbibition rules +binary diffusion in gas phase (no film effect)

sults presented in [5] for quasistatic fluid invasion, the IP algorithm is expected to represent a good model for modeling the capillary effects provided that the contact angle is not too close to 90°. For simplicity, we introduce an upper bound contact angle, denoted θ_{c2}, over which IP begins to represent a too poor approximation. As explained in [5], when θ approaches θ_{c2} cooperative mechanisms between neighboring throats (typically overlaps of neighbor menisci) become not negligible and this affects the invasion pattern since invasion is not controlled anymore only by the meniscus burst mechanism in the throat. This leads to distinguish three main regimes for slow evaporation in a hydrophilic pore network depending on the value of contact angle, assuming for simplicity that $\theta_c < \theta_{c2} < 90°$, which is representative of the experiments on etched networks presented in previous papers [16]. In regime I ($\theta < \theta_c$), film effects have to be taken into account and IP rules can be used. This regime can be simulated using the model presented in [12] or [13]. In regime II ($\theta_c < \theta < \theta_{c2}$), films can be neglected and IP rules are still acceptable. This is the simplest regime. It can be simulated using the model described in [6]. In regime III ($\theta_c < \theta_{c2} < \theta < 90°$), film effect is negligible but IP rules are not sufficient to model the menisci displacement. Noting, on the basis of the results presented in [5], that θ_{c2} is *a priori* close to 90°, we expect that regime III corresponds to a very narrow range of contact angles near 90°. As a result, we do not explore regime III in this paper. We mainly concentrate on regime II, which can be expected to be valid over a significant range of contact angles below 90°, but also get some insights into regime I (IP+film) using the drying pore network model with film described in [13]. These various regimes are summarized in Table I.

As described in [6], the evaporation algorithm used to simulate slow evaporation in regime II takes into account the capillary control of invasion by the IP rules and introduces a kinetic aspect through the computation of the diffusive transport into the gas phase and the mass flux at the boundary of each liquid cluster. More precisely the quasisteady diffusion equation $\Delta P_v = 0$ is solved in the part of the network occupied by the gas phase with the boundary conditions: $P_v = P_{ve}$ on the menisci, where P_{ve} is the equilibrium vapor partial pressure, and Eq. (1) at the entrance of ducts located along the open edge of the network, see [6] for more details.

For the sake of completeness, this drying algorithm is summarized here: (1) every liquid cluster present in the network is identified; (2) the interfacial element (throat) of greatest invasion potential (greatest capillary threshold) is identified for each cluster, the volume of liquid contained at time t in this throat and the adjacent pore is V_{sc}; (3) the evaporation flux F_c at the boundary of each cluster is computed from the finite volume computation of the liquid vapor partial pressure in the gas phase (obtained from the numerical solution of equation $\Delta P_v = 0$); (4) for each cluster, the time t_c required to evaporate the amount of liquid contained in the element identified in step (2) is computed: $t_c = \frac{\rho_\ell V_{sc}}{F_c}$; (5) the element among the elements selected in step (2) eventually invaded is that corresponding to $t_{c\,\min} = \min(t_c)$; and (6) the phase distribution within the network is updated, which includes the partial evaporation of liquid contained in the elements selected in step (2) with $\rho_\ell V_\ell(t + t_{c\,\min}) = \rho_\ell V_\ell(t) - F_c t_{c\,\min}$ (where ρ_ℓ is the liquid density and V_ℓ the volume of liquid contained in the element) except for the element selected in step (5) which becomes completely saturated by the gas phase. The procedure can be repeated up to full drying of the network or stopped at some intermediate stage.

In the case of ducts of rectangular cross section, the throat invasion potential [step (2)] reads [18]

$$P_{ct} = 2\gamma \cos\theta \left[\frac{1}{e} + \frac{1}{d} \right]. \tag{2}$$

C. Hydrophobic network

The present work deals with evaporation on hydrophobic pore networks. We proceed by analogy with the hydrophilic situation. Since in the quasistatic limit the capillary effects during evaporation can be modeled using IP rules as in the quasistatic mechanical displacement corresponding to the

displacement of a wetting fluid by a nonwetting one (this process is usually called drainage), we expect that capillary effects during evaporation in a hydrophobic network can be modeled as in the mechanical displacement corresponding to the displacement of a nonwetting fluid by a wetting one (this process is usually called imbibition). Thus we rely on the analysis of the imbibition process as far as hydrophobic networks are concerned. Since the work of Lenormand and Zarcone [18], it is well-known that imbibition in a network can be a significantly more complex displacement process than drainage. Whereas in drainage (when $\theta < \theta_{c2}$) the invasion is controlled by the throat invasion mechanism only, throat invasion and pore invasion mechanisms should be distinguished in imbibition and the process may also depend on film flows and snap-off phenomena. This can lead to a variety of invasion patterns, e.g., [18,19]. Similarly as in the hydrophilic situations, we can expect that the film effects can be neglected when the contact angle of the wetting phase (the gas phase for the hydrophobic network) is higher than some critical value (45°, for example, in the network of rectangular ducts). Although very high contact angle of the dense phase close to 180° can be obtained on rough superhydrophobic surfaces [20], the equilibrium contact angle (measured in liquid water) is generally lower on ordinary hydrophobic surfaces, such as teflonized or silanized ones, with a contact angle θ of the order of 110°–120° (which corresponds to contact angles of the order of 60°–70° for the gas phase). Thus we consider contact angles in this range as regards to hydrophobic networks, noting that film effects can be generally neglected for such values of contact angles. It could be argued that liquid film flow can develop due to smaller scale defects (wall roughness, etc.). This has not been taken into consideration, however, in this study. Film effects are therefore neglected in the modeling of evaporation in the hydrophobic network.

Under these circumstances, the simulation of evaporation in a hydrophobic network becomes analogous to the hydrophilic case. The essential difference is that pore and throat invasion must be considered as two distinct mechanisms (in the hydrophilic case under IP rules invasion of a throat leads automatically to the invasion of the adjacent pore whereas in the hydrophobic case the invasion of the pore is a distinct event), which implies the need to define pore invasion potentials in addition to the throat invasion potential. The potentials used in this work are presented in the Appendix.

Under these circumstances, simulating evaporation in the hydrophobic network can be performed using an algorithm analogous to the one developed for the hydrophilic case, i.e., it combines the computation of the water vapor partial pressure at each node of the gas phase and the mass flux at the boundary of each cluster with the rules describing an imbibition process. Only step (2) is to be modified and now reads: (2) the interfacial element (pore or throat) of greatest invasion potential (greatest capillary threshold) is identified for each cluster, the volume of liquid contained at time t in this element is V_{sc}.

D. Drying invasion patterns

Representative examples of drying patterns obtained numerically on a small network thanks to the algorithms summarized above are shown in Fig. 3. Whereas the invasion pattern is characteristic of an evaporation IP pattern in the hydrophilic network, the invasion pattern in the hydrophobic network is compact (no temporary trapped liquid clusters) and characterized by an almost flat traveling front. These patterns are fully consistent with the numerical results presented in [5] on the quasistatic invasion of a fluid in a model porous medium and in good agreement with experimental patterns (not shown here) obtained on a square network machined in a Plexiglas (hydrophilic network) or a Teflon™ (hydrophobic network) plate having the same local geometry as the one used for the simulations shown in Fig. 3, [21]. It is interesting to notice that the flat front in the hydrophobic network is only due to capillary effects and not to viscous or gravity stabilizing effects [17]. The occurrence of flat and compact patterns in the hydrophobic case can be explained from the hierarchy in the invasion potentials, see the Appendix.

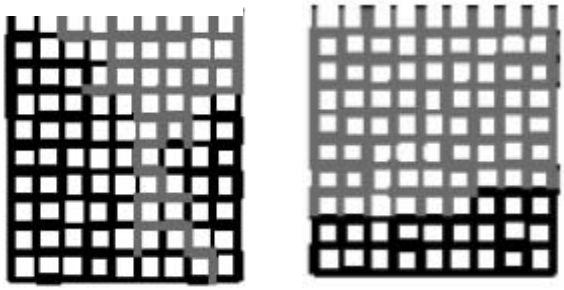

FIG. 3. Examples of evaporation patterns (liquid phase in black, gas phase in gray) (a) hydrophilic network and (b) hydrophobic network.

III. NUMERICAL STUDY OF SLOW DRYING

From the patterns presented above, it can be anticipated that the hydrophobic nature of the material has a significant impact on drying times compared to the hydrophilic case. The overall drying time for the hydrophobic case is *a priori* easy to estimate since this case reduces to a simple receding flat evaporation front at the boundary between a growing dry zone and a shrinking fully saturated liquid one. Thus we begin with estimating the overall drying time for a flat receding evaporation front. The evaporation mass flux density within the network can be estimated in this case as

$$j = \varepsilon_s D^* \frac{M_v}{RT} \frac{(P_{ve} - P_{vi})}{z_0}, \tag{3}$$

where $z_0(t)$, D^*, and ε_s are the front position (measured from the open edge of the network), the network effective vapor diffusion coefficient, and cross-section porosity, respectively. Then equating the mass flux density of liquid water evaporating with the mass diffusive flux density gives

$$\varepsilon \rho_\ell \frac{dz_0}{dt} = \varepsilon_s D^* \frac{M_v}{RT} \frac{(P_{ve} - P_{vi})}{z_0}, \tag{4}$$

where ε is the network overall porosity.

Combining Eqs. (1), (3), and (4) gives after integration

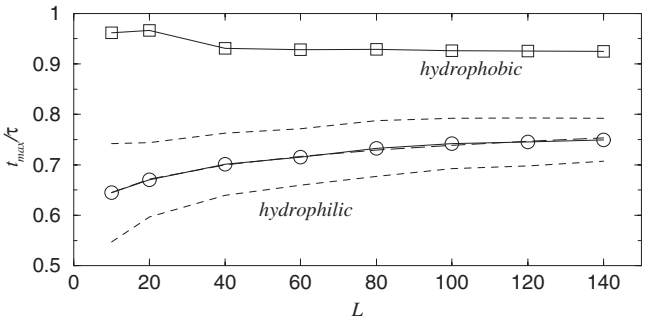

FIG. 4. Overall drying time for 2D hydrophilic and hydrophobic square networks as a function of network size. $t_{\max}=\tau_{\mathrm{nw}}$ (hydrophobic network) or $t_{\max}=\langle\tau_w\rangle$ (hydrophilic network). The dashed lines represent ±1 standard deviation of τ_w/τ obtained in numerical simulations.

$$0.5z_0^2+\frac{D^*}{D}\delta z_0-\frac{\varepsilon_s M_v D^* \Delta P_v}{\varepsilon RT\rho_\ell}t=0, \tag{5}$$

where $\Delta P_v=P_{ve}-P_{v\infty}$.

D^*, ε_s, and ε are estimated from pore network simulations for the square pore networks considered in this study. It is found $D^*\approx 0.97D$ (which is consistent with the fact that the square network is not tortuous), $\varepsilon_s\approx 0.5$, and $\varepsilon\approx 0.74$. As a reference time, we chose the overall drying time corresponding to drying when the external mass transfer resistance can be ignored ($\delta\ll L$), i.e., from Eq. (5) with $\delta=0$ and $z_0=L$,

$$\tau=\frac{\varepsilon RT\rho_\ell L^2}{2\varepsilon_s M_v D\Delta P_v}. \tag{6}$$

Taking the size of porous network L as reference length, Eq. (5) is expressed in dimensionless form as

$$z_0^{*2}+2\delta^* z_0^*-t^*=0, \tag{7}$$

which leads to

$$z_0^*=\sqrt{\delta^{*2}+t^*}-\delta^*. \tag{8}$$

Thus the overall drying time for the receding flat front model is given by

$$\tau_{\mathrm{ff}}^*=1+2\delta^*. \tag{9}$$

As generally in convective drying $\delta^*\ll 1$, $\tau_{\mathrm{ff}}^*\approx 1$, i.e., $\tau_{\mathrm{ff}}\approx\tau$.

However, this estimate of overall drying time does not agree exactly with the hydrophobic pore network simulations. As depicted in Fig. 4, $\tau_{\mathrm{nw}}/\tau\approx 0.93$, where τ_{nw} is the overall drying time for the hydrophobic network. This difference is attributed to the difference in the front moving mechanism. The front displacement is continuous in the receding flat front model whereas the displacement is by line discrete erosion in the hydrophobic network. An additional difference occurs at the end of drying when the last row of pore evaporates in the hydrophobic network. This can be seen in Fig. 5(a), which shows the evolution of the equivalent evaporation flat front position z_{feq}, which is defined as

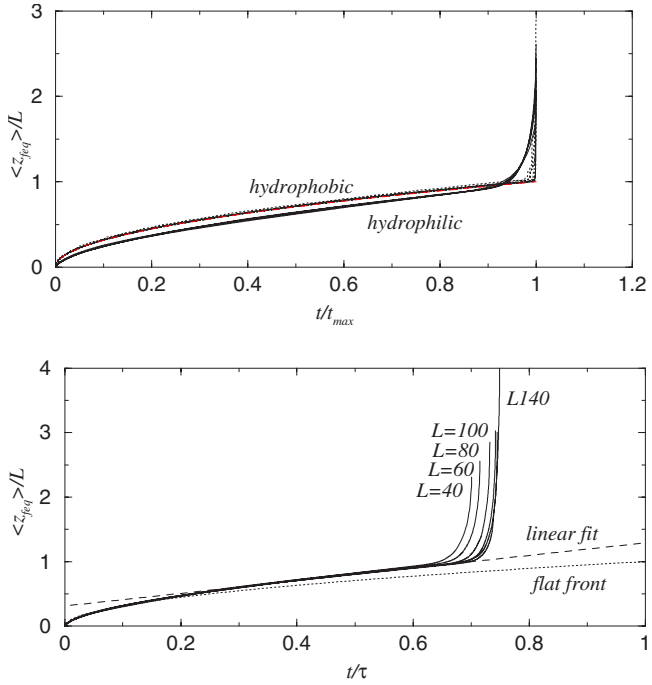

FIG. 5. (Color online) Evolution of average equivalent front position as a function of dimensionless time. Results are for $L=20$, 40, 50, 60, 80, and 100. $t_{\max}=\tau_{\mathrm{nw}}$ (hydrophobic network) or $t_{\max}=\langle\tau_w\rangle$ (hydrophilic network).

$$z_{\mathrm{feq}}=\frac{\varepsilon_s M_v D(P_{ve}-P_{v\infty})}{j_{nw}RT}, \tag{10}$$

where j_{nw} is the evaporation flux density in the hydrophobic network. Thus z_{feq} represents the position of the flat front that would lead to the same evaporation flux as in the hydrophobic network. As can be seen from Fig. 5, z_{feq} abruptly increases when the last row of pores evaporates. Hence one can distinguish two main drying periods. The first one up to $z_{\mathrm{feq}}/L\approx 1$ can be simulated using the flat front model provided that the effective diffusion coefficient is corrected. One can take $D^*\approx 0.97D\tau/\tau_{\mathrm{nw}}\approx 1.05D$. The second period corresponds to the abrupt increase of z_{feq}. This corresponds to an abrupt fall in the evaporation flux. We define the time t_1 marking the end of the first period as the time for which $\frac{z_{\mathrm{feq}}-z_{\mathrm{ff}}}{z_{\mathrm{ff}}}$ becomes for the first time greater than 1%, where z_{ff} is the flat front solution on which all the data collapse during the first period. As shown in Fig. 6, which shows the duration of the second period over the overall drying time, this second period becomes negligible for sufficiently large networks.

The situation is not as simple for the hydrophilic case since the drying rate depends both on the external driving evaporation potential, which varies as δ^{-1}, and the diffusive transfer within the network over a significant period of drying. This is illustrated in Fig. 7 which shows the evolution of overall drying time as a function of δ^*. In Fig. 7(a), τ_{ff} is used as the reference time whereas $t_{\mathrm{ref}}=\frac{\rho_\ell\varepsilon L^2 eRT\delta}{DM_v(P_{ve}-P_{v\infty})}$ is used in Fig. 7(b); t_{ref} would be the overall drying time if the vapor partial pressure at the network surface was P_{ve} over the

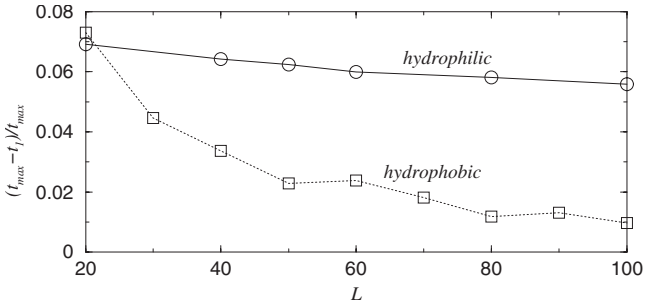

FIG. 6. Evolution of relative duration of last drying period as a function of network size. $t_{\max}=\tau_{\mathrm{nw}}$ (hydrophobic network) or $t_{\max}=\langle\tau_w\rangle$ (hydrophilic network); t_1 is the time marking the beginning of the last drying period.

whole drying (=drying controlled only by the external transfer). It is expected that the drying time tends toward t_{ref} as $\delta^* \to \infty$. As illustrated in Fig. 7(b), $\frac{\tau_w}{t_{\mathrm{ref}}}-1 \approx 0.35(\delta/L)^{-1}$ when $\frac{\delta}{L} \gg 1$. Although not impossible (for example, when drying occurs with a very high external relative humidity), this case is not common in convective drying since generally $\delta^* \ll 1$. Under these circumstances, Fig. 7(a) shows that the overall drying time becomes independent of the external transfer length scale when δ^* is sufficiently small, i.e., when $\delta/a \leqslant 10^{-2}$, where a is the lattice spacing. The average overall drying time $\langle\tau_w\rangle$ for hydrophilic networks has been computed over many realizations (see Table II) and various network sizes in this limit ($\delta/a \leqslant 10^{-2}$). The results are plotted in Fig. 4. The mean overall drying time for the hydrophilic network is significantly smaller than for the hydrophobic one over the range of size investigated: for example $\langle\tau_w\rangle/\tau_{\mathrm{nw}} \approx 0.8$ for $L=100$. This was expected since a flat front (~hydrophobic network) represents a very slow solution. The ratio $\langle\tau_w\rangle/\tau$ very slowly increases with network size L. The data can be reasonably fitted by a power law (long dashed line hardly visible in Fig. 4), which leads to a low exponent ≈0.06. Hence $\langle\tau_w\rangle$ scales as $\sim L^{2.06}$ over the range of sizes investigated. It is clear, however, that this scaling should not hold for very large sizes. How $\langle\tau_w\rangle/\tau$ varies with network size for larger sizes is investigated in the following.

As shown in Fig. 5(b), one can distinguish two main drying periods. During the first period, the equivalent flat front

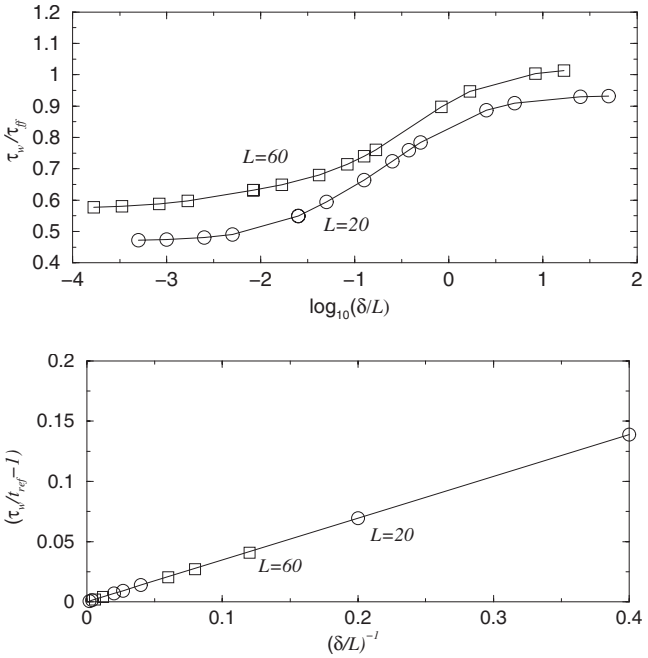

FIG. 7. Evolution of overall drying time as a function of external length scale δ^*.

position, Eq. (10), averaged over many realizations (see Table II) follows the flat front solution, i.e., $\langle z_{\mathrm{feq}}\rangle \propto t^{1/2}$. Then, after a crossover, the equivalent front position varies linearly with t. A best fit gives

$$\frac{\langle z_{\mathrm{feq}}\rangle}{L} = \frac{z_{\mathrm{li}}}{L} \approx 0.980\frac{t}{\tau} + 0.312. \tag{11}$$

Finally, as in the hydrophobic case, $\langle z_{\mathrm{feq}}\rangle$ also abruptly increases toward the end of drying when the last liquid clusters attached to the bottom of the network evaporate. Compared to a hydrophobic network of the same size, the relative duration of the second period is much greater, which is consistent with the IP mechanism leading to the formation of large liquid clusters. However, as shown in Fig. 6, the relative duration of the second period decreases, albeit very slowly, with network size. For the hydrophilic case, the time t_1 marking the end of the linear period is defined as the time for

TABLE II. Average and standard deviation of drying time, and minimum and maximum drying times as a function of network size. N is the number of realizations. σ is the standard deviation of τ_w over the number N of considered realizations.

L	N	$\langle\tau_w\rangle/\tau$	$(\tau_w/\tau)_{\min}$	$(\tau_w/\tau)_{\max}$	$\sigma/\langle\tau_w\rangle$
10	10 000	0.645	0.332	0.886	0.151
20	10 000	0.670	0.413	0.876	0.110
40	500	0.701	0.430	0.832	0.088
60	500	0.715	0.531	0.839	0.078
80	250	0.732	0.570	0.843	0.075
100	250	0.742	0.590	0.852	0.067
120	200	0.745	0.591	0.845	0.064
140	200	0.749	0.567	0.861	0.057

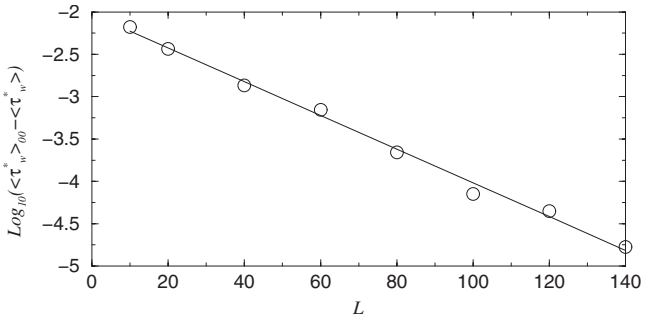

FIG. 8. Semi-log plot of $(\langle\tau_w\rangle/\tau)_\infty - \langle\tau_w\rangle/\tau$ as a function of system size.

which $\frac{\langle z_{\text{feq}}\rangle - z_{\text{li}}}{z_{\text{li}}}$ becomes greater than 5% for the first time. Thus the scale dependence of the dimensionless overall drying time is not due to this second period. Since the flat front solution represents an upper bound, the dimensionless overall drying time should reach a limit lower than 1 as the system size increases. We conjecture that the dimensionless overall drying time tends exponentially toward this limit as the system size increases, i.e.,

$$\frac{\langle\tau_w\rangle}{\tau} = \left(\frac{\langle\tau_w\rangle}{\tau}\right)_\infty - A_1 \exp\left(-A_2\frac{L}{a}\right), \tag{12}$$

where a is the lattice spacing. It should be noticed that viscous effects and/or gravity effects can become non-negligible as the system size increases, e.g., [17]. Again, throughout this paper, we are only interested in situations where capillary effects dominate the invasion. For $\left(\frac{\langle\tau_w\rangle}{\tau}\right)_\infty$, a best fit gives $\left(\frac{\langle\tau_w\rangle}{\tau}\right)_\infty \approx 0.756$. As can be seen from Fig. 8, our numerical data are in good agreement with an exponential decay of $\left(\frac{\langle\tau_w\rangle}{\tau}\right)_\infty - \frac{\langle\tau_w\rangle}{\tau}$ with L. The linear fit shown in Fig. 8 gives $A_1 \approx 0.137$ and $A_2 \approx 0.022$.

As shown in Fig. 9, the distribution of τ_w for a given network size is not exactly Gaussian. In particular, the distribution is not symmetric with a right skew. This is observed for all network sizes considered in this study with a skewness of ~0.35 and a kurtosis of ~2.7, thus lower than 3. As also shown in Fig. 4, the ratio $\sigma_\tau/\langle\tau_w\rangle$, where σ_τ is the standard deviation of τ_w, is quite high and tends to decrease slowly with network size L. This indicates a significant variation in drying time from one realization to the other. This can also be seen from Table II, which shows the minimum and maximum of τ_w/τ over the number of realizations considered for each network size.

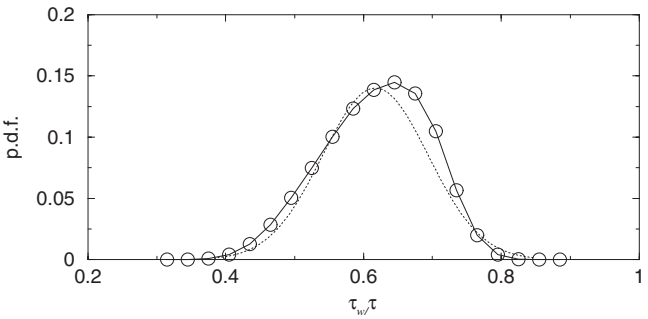

FIG. 9. Representative example of PDF (probability density function) of overall drying time τ_w for a hydrophilic network (results are for 100 000 realizations of a 15×15 network). The dashed line represents a Gaussian distribution.

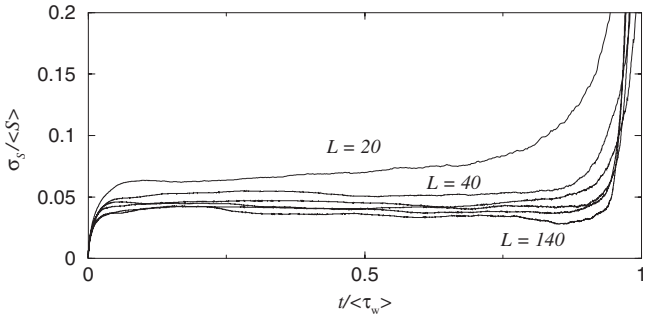

FIG. 10. Evolution of the standard deviation of saturation σ_S as a function of dimensionless time for network size $L=20$, 40, 50, 60, 80, 100, and 140.

The fluctuations of overall saturation (≈fraction of pores occupied by the liquid phase in the network) with the realizations are also significant except at the very beginning of drying. This is illustrated in Fig. 10 which shows the evolution of the standard deviation of saturation σ_S as a function of time for three network sizes. Note that the ratio $\sigma_S/\langle S\rangle$ tends to become a constant over most of the drying for sufficiently large networks. This constant decreases with network size. Finally, Fig. 11 shows the evolution of the average saturation as a function of time for three system sizes. As can be seen from Fig. 11, the plots for $L=80$, 100, and 140 are

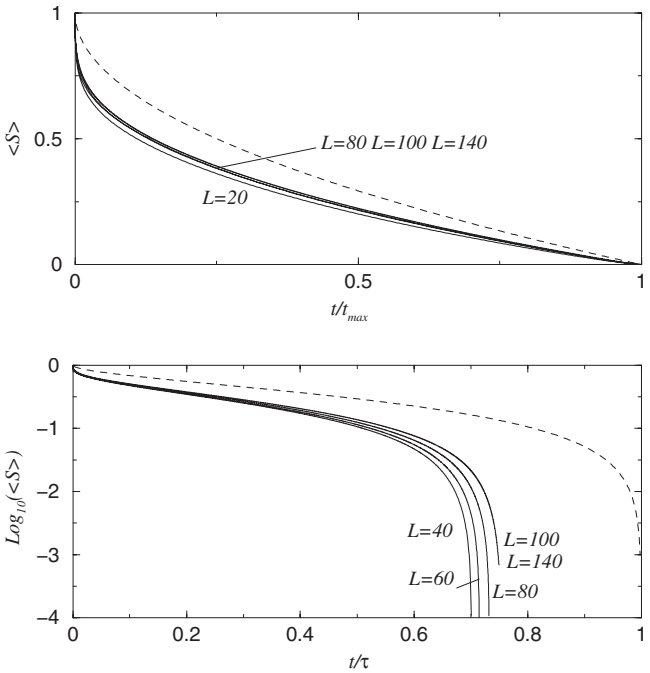

FIG. 11. Evolution of the overall average saturation as a function of reduced time for various system sizes. The dashed line represents the flat front solution. $t_{\max}=\tau$ (flat front solution) or $t_{\max}=\langle\tau_w\rangle$ (hydrophilic network).

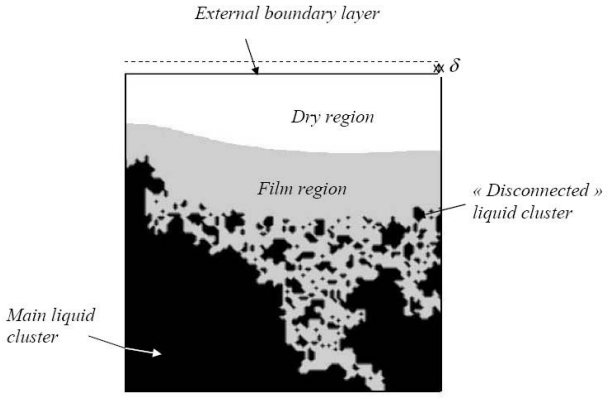

FIG. 12. Sketch of phase distribution during the drying process in a hydrophilic network in the presence of film (regime I); fully saturated liquid region in black, film region in gray, and dry region in white.

hardly discernible except at the very end of drying corresponding to the third period. The fact that the average drying behavior can be characterized with a single curve for a sufficiently large network is consistent with the fact that the network size L is the unique length in the problem (in the limit $\delta^* \ll 1$). A similar behavior was already observed for the average equivalent front position z_{feq} (Fig. 5). Naturally, z_{feq}, i.e., the evaporation flux at the porous surface, also significantly fluctuates from one realization to the other. This reflects the variation in the invasion pattern with each realization.

The results presented are for 2D networks of aspect ratio 1, i.e., $L/W=1$, where W is the width of network and L its length. It is expected that $\langle \tau_w \rangle / \tau \to 1$ as $L/W \to \infty$ since the width introduces an upper cutoff in the development of large capillary digitations. It is also expected that $\left(\frac{\langle \tau_w \rangle}{\tau}\right)_{L/W<1} < \left(\frac{\langle \tau_w \rangle}{\tau}\right)_{L/W=1}$. The detailed study of drying for networks of aspect ratio different from 1 is left for a future work.

IV. FILM EFFECTS ON DRYING TIME FLUCTUATIONS IN HYDROPHILIC NETWORKS

As discussed in the Introduction, the liquid film effect has to be taken into account when $\theta < \theta_c$ (regime I). The primary effect of liquid film is to reduce the overall drying time since liquid films represent a transport mechanism from the liquid clusters that is much more efficient than diffusion in gas phase. This has been shown experimentally with etched networks [16], and is in qualitative agreement with recent pore network models of drying including the film effect [12,13]. As discussed in [13], two main subregimes can be distinguished within regime I. Subregime 1 is when the films develop up to the network entrance over the whole (or most of) drying. Under these circumstances, one expects a constant drying rate all over drying, which only depends on the external conditions. Subregime 2 is when the film tip region recedes into the network during drying (see Fig. 12). Suppose the conditions (network size, external conditions, network pore geometry) are such that the system goes from subregime 1 to regime II (no film) as the contact angle θ varies up to θ_c. Suppose that θ_{c1} is the contact angle marking the transition from subregime 1 to subregime 2. Thus for $\theta < \theta_{c1}$, we expect that the overall drying time is not sensitive to the detail of the invasion pattern but only to the initial mass of liquid present in the network. As this initial mass slightly varies with each realization, one still expects small overall drying time fluctuations in this subregime, but significantly less than in regime II. Therefore we expect that the magnitude of the overall drying time fluctuations increases as θ varies from θ_{c1} to θ_c. To illustrate this, we have performed simulations for 1000 realizations of a 20×20 network using the drying pore–network model with film described in [13]. In this model, the variable characterizing the film is its local curvature radius R in the duct cross section. The equation governing R^3 is shown to be of the same Laplacian form as the diffusion equation in gas phase governing the vapor partial pressure P_v in the dry (no film) region of pore space. Introducing a composite variable Φ which is a linear combination of R^3 and P_v makes it possible to describe the transport both in the film region and the dry region (see Fig. 12) with an equation of the form $\Delta\Phi=0$. Under these circumstances, the algorithm becomes completely similar to the one presented in Sec. II B. Only step (3) is modified and reads: (3) the flux F_c at the boundary of each cluster is computed from the finite volume computation of Φ in the film region and/or dry region (obtained from the numerical solution of equation $\Delta\Phi=0$). One can refer to [13] for the details.

The magnitude of drying time fluctuations is measured using the two following indicators:

$$\sigma^*_\theta = \frac{[\sigma_{\tau_w}/\langle \tau_w \rangle]_\theta}{[\sigma_{\tau_w}/\langle \tau_w \rangle]_{\theta_c}}, \tag{13}$$

$$\Delta t^*_w = \frac{[(\tau_{w\,\max} - \tau_{w\,\min})/\langle \tau_w \rangle]_\theta}{[(\tau_{w\,\max} - \tau_{w\,\min})/\langle \tau_w \rangle]_{\theta_c}}, \tag{14}$$

where σ_{τ_w}, $\tau_{w\,\max}$, and $\tau_{w\,\min}$ represent the standard deviation, maximum, and minimum of the overall drying time over the 1000 realizations, respectively. Results are shown in Fig. 13. Note the drastic reduction of average drying time as $\theta \to \theta_{c1}$. As expected, Fig. 13 illustrates the fluctuation damping effect due to films. A similar effect is expected for larger networks except for the fluctuations due to initial liquid content variations (visible when $\theta \to \theta_{c1}$ in Fig. 13), which are expected to vanish as the network size increases. From this, one can conclude that the magnitude of overall drying time fluctuations could be an indication of the importance or not of film effect in drying experiments involving several samples of the "same" materials.

V. CONCLUSIONS

In this paper, we have studied slow evaporation in hydrophobic or hydrophilic 2D model porous media over limited ranges of contact angle, i.e., under conditions for which film effects are negligible in hydrophobic networks and the IP algorithm represents a satisfactory model of quasistatic

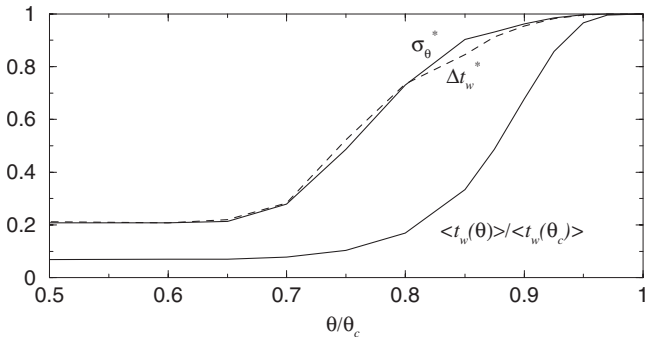

FIG. 13. Influence of film in hydrophilic network. Evolution of average overall drying time, overall drying time standard deviation, and maximum variation as a function of apparent contact angle θ. Results are for 1000 realizations of a 20×20 network. Film influence decreases as θ/θ_c increases above $\theta/\theta_c\approx0.6$. For $\theta/\theta_c<0.6$, liquid film extends up to the entrance of the network all over drying. For $\theta/\theta_c\geqslant1$, liquid film cannot develop and the transport mechanism of water from the liquid clusters is by diffusion in gas phase only.

drainage in the hydrophilic ones. It has been shown how evaporation in the hydrophobic network can be simulated using the imbibition invasion rules and predicted analytically using a moving flat front solution. Then we have conducted a numerical statistical study of drying in 2D networks when the external transfer resistance is negligible. As expected, drying in hydrophilic networks is faster than in hydrophobic ones. For the networks of aspect ratio 1 studied in this paper, the dimensionless average overall drying times tend toward 0.93 and 0.75 as the size of the network increases in hydrophobic and hydrophilic networks, respectively. Thus drying is 20% faster on average in a hydrophilic network compared to a hydrophobic one. However, drying in hydrophilic networks is subject to important fluctuations owing to the spatial fluctuations in the invasion percolation pattern associated with each realization. It has been shown that the overall drying time distribution in hydrophilic networks is nearly Gaussian with a right skew. The fluctuations diminish with system size but are significant for all sizes considered in the present work leading to maximum relative variations of more than 25% in the drying time with the realizations. Except during the very last period of drying which is system size dependent, the average behaviors can be described by master curves. Finally simulations in the hydrophilic network including the effect of liquid films indicate a damping of the fluctuations when the film effect is significant.

ACKNOWLEDGMENT

Financial support from 5th PCRD European program FEBUSS is gratefully acknowledged.

APPENDIX

We present in this appendix the algorithm used to simulate the imbibition process in the network. As first analyzed in [18] the filling of throat and the filling of pores must be considered as two distinct steps in the invasion process. Also, two types of advances can be distinguished. The first is pistonlike, where the fluid advances in a connected front occupying the centers of the pore space. The second is induced by the wetting fluid flow along crevices in the pore space (the corner of the throat in our idealized porous system) and leads to pores filling in advance of the connected front through the snap-off mechanism [18,19]. As discussed before, the flow along the corner is only possible below the critical contact angle θ_c and therefore the snap-off mechanism can be ignored in our case. Thus we are only interested here in the pistonlike type of advance. The capillary pressure threshold for a pistonlike advance in a throat of rectangular cross section is given by

$$P_{\mathrm{ct}}=2\gamma\cos\theta_w\left[\frac{1}{e}+\frac{1}{d}\right], \tag{A1}$$

here γ is the surface tension, θ_w ($\theta_w=\pi-\theta$) is the contact angle of the wetting fluid (gas phase in our case), e is the throat depth, and d is the throat width.

The filling of the pore is more complex [18,19]. The pore filling threshold curvature is dependent on the number of surrounding throats filled with wetting fluid. For a lattice of coordination number z, there are z such imbibition mechanisms, called I_0 to I_{z-1}, which represent filling of a pore when zero to $z-1$ connecting throats contain nonwetting fluid. The I_0 mechanism can only occur if the nonwetting fluid is compressible. It is ignored here since liquid water is the nonwetting fluid in a hydrophobic system. The capillary pressures are ranked $P_{\mathrm{cp}}(I_i)>P_{\mathrm{cp}}(I_{i-1})$. In our case, $z=4$ and therefore we have to consider mechanisms I_1 to I_3 with $P_{\mathrm{cp}}(I_1)>P_{\mathrm{cp}}(I_2)>P_{\mathrm{cp}}(I_3)$. Expressions for $P_{\mathrm{cp}}(I_i)$, $i=1,3$ were given by Lenormand and Zarcone [18] for the special case where all surrounding throats have the same width and the same depth. For the present study, we have taken into account the variations in width of the surrounding throats and considered contact angles representative of the air, water, and Teflon systems. The pore capillary threshold is expressed as

$$\frac{P_c(I_i)}{\gamma}=\pm\frac{1}{R_c}+\frac{2\cos\theta_w}{e}, \tag{A2}$$

where R_c is the main curvature radius of the pore meniscus in the plane of the network. R_c is taken positive. In the right-hand side (rhs) of Eq. (A2), the + sign applies to the I_1 mechanism whereas the − sign applies to I_2 and I_3 mechanisms. The second term in the rhs of Eq. (A2) represents the contribution of the meniscus curvature in the pore depth. Expressions for $R_c(I_i)$ were derived for the pore shape of our network and evaluated for a contact angle corresponding to water on Teflon. They are summarized in what follows, see [21] for more details. The method is to study the evolution of the curvature radius of the menisci within the pores until they touch each other or one of the growing meniscus inside the pore touches a solid wall. Using the notations shown in Fig. 14, $R_c(I_1)$ is expressed as

$$R_c(I_1)=\min(R_j),\quad j=1,4, \tag{A3}$$

with $R_j=\sqrt{x_j^2+y_j^2}$ where (x_j,y_j) are the coordinates of pore corners using the barycenter of the pore four corners as the

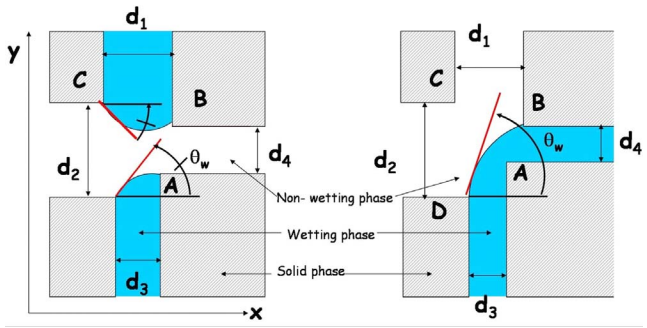

FIG. 14. (Color online) Sketch of I_{2o} and I_{2a} pore invasion mechanisms.

origin of the local (x,y) Cartesian coordinates system.

For the I_2 mechanism, one has to distinguish two cases depending on the relative position of the throats containing the nonwetting fluids. As depicted in Fig. 14, the first one is when the throats are adjacent, and the second is when the throats are opposite each other. Assuming that the wetting fluid is in the throats numbered 3 and 4 in Fig. 14, $R_c(I_2)$ for the adjacent case is given by

$$R_c(I_{2a}) = \max[R(I_{21}), R(I_{22})], \tag{A4}$$

where the expressions for $R(I_{21})$ and $R(I_{22})$ read

$$R(I_{21}) = \frac{1}{4}\left(\frac{(d_1+d_3)^2+(d_2+d_4)^2}{\sin\theta_w(d_2+d_4)-\cos\theta_w(d_1+d_3)}\right), \tag{A5}$$

$$R(I_{22}) = \frac{1}{4}\left(\frac{(d_1+d_3)^2+(d_2+d_4)^2}{\sin\theta_w(d_1+d_3)-\cos\theta_w(d_2+d_4)}\right). \tag{A6}$$

When the throats are opposite each other, there are two options: (i) the menisci curvature radius reaches a minimum before the two opposite menisci touch each other and (ii) the invasion proceeds until contact with the opposite menisci. In our case, option (ii) is much more unlikely than option (i). For simplicity, only option (i) is considered in the simulation. Option (ii) is in fact similar to two I_3 mechanisms. Thus one can use the expression derived for the I_3 mechanism, which is given below. This leads to two minimum radii of curvature $R_c(I_{3t})$ and $R_c(I_{3b})$ (for top and bottom in Fig. 14). $R_c(I_{2o}) = \max[R_c(I_{3t}), R_c(I_{3b})]$. For the I_3 mechanism, it is found

$$R_c(I_3) = \frac{d_3^2 + 0.25(d_2-d_4)^2}{2d_3\sin\theta_w - \cos\theta_w(d_2-d_4)}. \tag{A7}$$

To simulate imbibition, the algorithm is as follows: (1) each element (pore or throat) saturated by the nonwetting fluid, not trapped and adjacent to a meniscus, is identified. This forms a list of interfacial elements that can be invaded; (2) invasion potential (=capillary pressure threshold as described above) is computed for each interfacial element; (3) the interfacial element of greatest potential is selected and invaded; and (4) return to (1) or stop if breakthrough is reached.

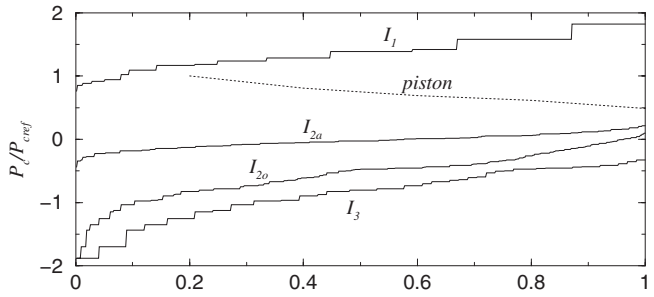

FIG. 15. Possible values of invasion potential in imbibition. For the pore invasion mechanisms, these values are computed by considering all possible combinations of nonwetting fluid occupied bond widths among the five possible values of throat width ($d = d_{\min} = 0.3$ mm, $d = 0.4$ mm, $d = 0.5$ mm, $d = 0.6$ mm, and $d = d_{\max} = 0.7$ mm). This represents a maximum of $n_{c\,\max} = 5^4$ configurations. Each potential is computed for each configuration and the values of the considered potential are ranked in increasing order. If i is the rank of a ranked potential value, the x-label is $x = i/n_{c\,\max}$. The reference potential is the greatest piston potential, i.e., $P_{\text{cref}} = P_{\text{ct}}(d_{\min}, e)$ with $e = 1$ mm.

The occurrence of flat and/or compact patterns can be explained from the hierarchy in the invasion potentials that is deduced from Eqs. (A1)–(A7). For the system considered in the present paper, the hierarchy is as follows:

$$P_c(I_1) > P_{\text{ct}} > P_c(I_{2a}) > P_c(I_{2o}) > P_c(I_3). \tag{A8}$$

This represents the most likely hierarchy. As illustrated in Fig. 15, this hierarchy is not strict as regards $P_c(I_{2a})$, $P_c(I_{2o})$, and $P_c(I_3)$. Starting from a fully saturated network, the invasion begins with a series of throat piston displacements leading to the invasion of all bonds connected to the network boundary. At this stage, all interfacial pores have three adjacent bonds occupied with nonwetting fluid. The next step is therefore the pore invasion associated with the most favorable I_3 mechanism, followed by the invasion of the three nonwetting fluid saturated bonds adjacent to this pore since throat piston potentials are greater than I_3 potentials. This leads to the possibility of I_{2a} mechanisms in addition to I_3 mechanisms. Since the I_{2a} potentials are generally greater than I_3 potentials, this leads to the filling of the first pore row by a succession of I_{2a} mechanisms and throat piston displacements. Occasionally, the pore invasion mechanism can be I_3 since $\max[P_c(I_3)] > \min[P_c(I_{2a})]$. Once the first row is invaded, the next rows are invaded one after the other as the first row by a succession of I_{2a} and throat piston mechanisms with occasional I_3 mechanisms. Although more favorable in terms of potential, the I_1 mechanism never occurs for the invasion scenario never leads to the formation of I_1 configuration.

[1] A. G. Yiotis, A. K. Stubos, A. G. Boudouvis, I. N. Tsimpanogiannis, and Y. C. Yortsos, Transp. Porous Media **58**, 63 (2005); A. G. Yiotis, I. N. Tsimpanogiannis, A. K. Stubos, and Y. C. Yortsos, J. Colloid Interface Sci. **297**, 738 (2006); T. Metzger, E. Tsotsas, and M. Prat, *Modern Drying Technology* (Wiley, New York, 2007), Vol. 1, Chap. 2.
[2] M. Prat, Chem. Eng. J. **86**, 153 (2002).
[3] A. Goudie and H. Viles, *Salt Weathering Hazards* (Wiley, Chichester, 1997).
[4] C. Y. Wang, in *Handbook of Fuel Cells*, edited by W. Vielstich, H. A. Gasteiger, and A. Lamm (Wiley, New York, 2003), Vol. 3, Part 3, p. 337.
[5] M. Cieplak and M. O. Robbins, Phys. Rev. B **41**, 11508 (1990); N. Martys, M. Cieplak, and M. O. Robbins, Phys. Rev. Lett. **66**, 1058 (1991).
[6] M. Prat, Int. J. Multiphase Flow **19**, 691 (1993).
[7] T. M. Shaw, Phys. Rev. Lett. **59**, 1671 (1987).
[8] D. Wilkinson and J. F. Willemsen, J. Phys. A **16**, 3365 (1983).
[9] M. Prat, Int. J. Multiphase Flow **21**, 875 (1995).
[10] A. G. Yiotis, A. K. Stubos, A. G. Boudouvis, and Y. C. Yortsos, Adv. Water Resour. **24**, 439 (2001).
[11] H. P. Huinink, L. Pel, M. A. J. Michels, and M. Prat, Eur. Phys. J. E **9**, 487 (2002); F. Plourde and M. Prat, Int. J. Heat Mass Transfer **46**, 1293 (2003).
[12] A. Yiotis, A. G. Boudouvis, A. K. Stubos, I. N. Tsimpanogiannis, and Y. C. Yortsos, Phys. Rev. E **68**, 037303 (2003); AIChE J. **50**, 2721 (2004).
[13] M. Prat, Int. J. Heat Mass Transfer **50**, 1455 (2007).
[14] D. S. de Freitas and M. Prat, Transp. Porous Media **40**, 1 (2000).
[15] Y. Le Bray and M. Prat, Int. J. Heat Mass Transfer **42**, 4207 (1999); L. A. Segura and P. G. Toledo, Chem. Eng. J. **111**, 237 (2005); A. G. Yiotis, I. N. Tsimpanogiannis, A. K. Stubos, and Y. C. Yortsos, J. Colloid Interface Sci. **297**, 738 (2006).
[16] J. B. Laurindo and M. Prat, Chem. Eng. Sci. **51**, 5171 (1996); **53**, 2257 (1998).
[17] M. Prat and F. Bouleux, Phys. Rev. E **60**, 5647 (1999); I. N. Tsimpanogiannis, Y. C. Yortsos, S. Poulou, N. Kanellopoulos, and A. K. Stubos, *ibid.* **59**, 4353 (1999).
[18] R. Lenormand and C. Zarcone, SPE 13264 (1984).
[19] M. J. Blunt and H. Scher, Phys. Rev. E **52**, 6387 (1995).
[20] J. Bico, C. Marzolin, and D. Quéré, Europhys. Lett. **47**, 220 (1999).
[21] O. Chapuis, Ph.D. thesis, INPT, 2006 (unpublished) (in French).